CrossMark

ORIGINAL PAPER

One-pot fabrication of single-crystalline octahedral Pd-Pt nanocrystals with enhanced electrocatalytic activity for methanol oxidation

Meiling Peng[1] · Wei Xu[1] · Weihao Cui[1] · Tao Wang[1] · Sheng Wang[1]

Abstract This study reports the synthesis of octahedral Pd-Pt bimetallic alloy nanocrystals through a facile, one-pot, templateless, and seedless hydrothermal method in the presence of glucose and hexadecyl trimethyl ammonium bromide. The morphologies, compositions, and structures of the Pd-Pt nanocrystals were fully characterized by various physical techniques, thereby demonstrating their highly alloying octahedral nanostructures. The formation or growth mechanism of the Pd-Pt bimetallic alloy nanocrystals was explored and is discussed here based on the experimental observations. In addition, the synthesized Pd-Pt nanocrystals were applied to the methanol oxidation reaction (MOR) in alkaline media, which proved that the as-prepared catalysts exhibit enhanced electrocatalytic activity for MOR. Pd_1Pt_3 exhibited the best stability and durability, and its mass activity was 3.4 and 5.2 times greater than those of Pt black and Pd black catalysts, respectively. The facile synthetic process and excellent catalytic performance of the as-prepared catalysts demonstrate that they have the potential to be used in direct methanol fuel cell techniques.

Electronic supplementary material The online version of this article (doi:10.1007/s10008-016-3370-9) contains supplementary material, which is available to authorized users.

✉ Tao Wang
  taotao571@hotmail.com

✉ Sheng Wang
  wangsheng571@hotmail.com

[1] Key Laboratory of Advanced Textile Materials and Manufacturing Technology, Ministry of Education, Zhejiang Sci-Tech University, Hangzhou 310018, People's Republic of China

Introduction

The intense development of fuel cells, which represent an alternative energy conversion technology to traditional fossil fuels, has brought this technology close to pre-commercial viability [1–4]. Also, Pt and Pt-based nanomaterials with unique physical and chemical properties have drawn significant attention because of their wide potential applications in electrocatalysis, fuel cells, and the petrochemical industry [5–7]. However, there is still a long way to go before these nanomaterials can be applied in practical applications, due to their low resistance to CO poisoning and the skyrocketing price of Pt [8, 9]. To this end, much research effort has been devoted to the development of highly active catalysts possessing long-term stability. Introducing a second metal to form Pt-M (i.e., Pd, Au, Co, Ni, Fe, or Cu) bimetallic nanocrystals is attractive for a wide variety of catalytic and electrocatalytic applications, as these applications can exhibit not only a combination of the properties associated with both metals but also enhancement or synergy due to strong coupling between the two metals [10–13].

Among various Pt-M bimetallic nanocrystals, Pt-Pd is the most well-studied system. There are various advantages of choosing Pd as a counterpart to Pt. Firstly, Pd is less expensive and more abundant than Pt. Pt and Pd share the same face-centered cubic (fcc) structure and an almost identical lattice constant (with a mismatch of only 0.77 %), and this similarity aids the formation of bimetallic nanocrystals with single crystallinity. Secondly, Pd is itself a high-performing catalyst in many industrial applications. Combining Pd and Pt can further enhance their catalytic performance for an existing reaction or lead to unexplored applications owing to the synergy between these two metals. Finally, using Pd instead of other metals such as Cu, Ag, Co, or Ni may also help to minimize catalyst corrosion and loss [12]. The last few years have witnessed the

Springer

preparation of many Pt-Pd bimetallic nanocrystals with a rich variety of structures and shapes, such as core–shell structures [14], nanocages [15], nanowires [16], nanodendrites [4], icosahedra [17], tetrahedra [18], and cubes [19]. Many methods of preparing these nanocrystals have been developed, such as co-chemical reduction [16], seed-mediated growth [20], electrochemical deposition [21], and galvanic replacement [22].

The abovementioned synthesis of specific nanostructured Pt-Pd bimetallic nanocrystals is highly desirable and potentially technologically important. For instance, numerous papers have addressed the methanol oxidation reaction (MOR) on Pt-Ru catalysts in acidic media in relation to the application of direct methanol fuel cells. Wang et al. fabricated Pd-Pt nanocages that showed high catalytic activity towards MOR, and the mass activity of the nanocages was about 5.3 times greater than that of commercial Pt black in acidic media [15]. Yamauchi et al. prepared core–shell Pd@Pt concave nanoparticles that had a current density 4.2 times higher than that of commercial Pt black in acidic media [14]. However, few works have addressed the MOR on Pt-based catalysts in alkaline media. Recently, in an in-depth investigation of the MOR, the use of alkaline electrolytes was found to offer several advantages, including a significantly wider range of electrode materials that are stable in alkaline media, and higher electrocatalytic activity for the oxidation of organic fuels in comparison with their activity in acidic media [23–25]. Kadirgan et al. investigated the electrocatalytic oxidation of methanol on Pt-Pd alloy electrodes with different compositions in alkaline solutions. It was reported that the exchange current densities of Pt-Pd catalysts for the MOR presented a pronounced maximum for a surface composition of about 15 % in palladium, and this enhanced MOR electroactivity was explained on the basis of a decrease in electrode poisoning [26]. Feng et al. obtained well-dispersed porous Pt-Pd nanodendrites through a wet chemical method by using urea as the structure-directing agent; the nanodentrites showed enhanced performance for MOR in alkaline media and a catalytic current density that was 3.05 times higher than that of Pt-black catalysts [4]. Strbac et al. reported a bimetallic electrode obtained by the deposition of Pd nanoislands on polycrystalline platinum, and concluded that a Pd:Pt ratio of 1:2 resulted in the strongest activity towards MOR in alkaline media [27].

Despite those successful demonstrations, studies on Pt-Pd bimetallic catalysts with different morphologies for the MOR in alkaline media are still lacking. Furthermore, most of the methods used to prepare these catalysts are either toxic or complicated. Therefore, it would be useful to identify more economic, facile solution-phase approaches in the synthesis of Pt-Pd nanostructures and to study their electroactivity in alkaline media.

In the work reported in the present paper, we developed a facile and environmentally friendly one-pot hydrothermal method to synthesize octahedral Pd-Pt nanocrystals by using glucose as the reducing agent and cetyltrimethylammonium bromide (CTAB) as the structure-directing agent. The electrocatalytic properties of Pd-Pt were investigated in alkaline media, with MOR employed as a model system.

Experimental

Chemicals and materials

Chloroplatinic acid ($H_2PtCl_6 \cdot 6H_2O$) and sodium tetrachloropalladate (Na_2PdCl_4) were purchased from Aladdin Reagents (Shanghai, China). Glucose, cetyltrimethylammonium bromide (CTAB), methanol (≥ 99.9 wt%), ethanol (≥ 99.7 wt%), and $HClO_4$ ($\simeq 70$–72 wt%) were commercially available from the Shanghai Chemical Reagent Co. Ltd. (Shanghai, China). Nafion (5 wt%) was purchased from Sigma–Aldrich (St. Louis, MO, USA). Commercial Pt black catalyst (with 60 % platinum loading) was purchased from Johnson Matthey (Royston, UK). Commercial Pd black was obtained from Alfa Aesar (Ward Hill, MA, USA).

Preparation of octahedral Pd-Pt nanocrystals

In a typical synthesis, $H_2PtCl_6 \cdot 6H_2O$ (0.2 M, 0.1 mL), Na_2PdCl_4 (0.2 M, 0.1 mL), an aqueous solution of glucose (0.5 M, 40 mL), and CTAB (50 mM, 5 mL) were mixed together and stirred to form a homogeneous solution. The molar ratio of the Pd and Pt precursors were adjusted according to the experimental requirements. Then the mixed solution was added to a Teflon liner and transferred to a stainless-steel autoclave. The autoclave was then heated to 180 °C for 1 h before being cooled to room temperature. The products were isolated by centrifugation at 6000 rpm for several minutes and were further washed three times with ethanol and water.

Characterization of the Pd-Pt nanocrystals

Transmission electron microscopy (TEM) samples were prepared by suspending the nanoparticles in ethanol and then casting on a holey carbon-coated Cu grid. High-resolution TEM images were obtained with a JEM-2010 (HR) instrument (JEOL, Tokyo, Japan) operating at 200 kV. Energy-dispersive X-ray analysis (EDX, Inca Energy-200) was used to investigate the compositions of the samples. X-ray diffraction (XRD) patterns were obtained on a D/MAX-RB X-ray diffractometer (D/Max-2550pc) using Cu-K$_\alpha$ radiation at a scan rate (2θ) of 0.05°/s, and were then used to determine the phase structure of each sample. The accelerating voltage and the applied current were 15 kV and 20 mA, respectively. Elemental analysis of the samples was carried out by X-ray photoelectron spectroscopy (XPS, K-Alpha, Thermo

Scientific, Waltham, MA, USA), using a monochromatized Al-Kα X-ray source operated at 12 kV and 20 mA. High-angle annular dark-field scanning TEM (HAADF-STEM) characterizations were performed with an FEI (Hillsboro, OR, USA) Tecnai G2 F30 S-Twin transmission electron microscope operating at 200 kV. The metal contents of the catalysts were measured using ICP-OES (Optima 2100 DV; PerkinElmer, Waltham, MA, USA).

Electrochemical performance characterization of the Pd-Pt nanocrystals

All the electrochemical experiments were performed on the electrocatalysts by using an electrochemical workstation (CHI660E, Chen Hua, Shanghai, China). Cyclic voltammetry (CV) and chronoamperometry were employed using a conventional three-electrode cell system with a glassy carbon electrode (GCE, $d = 3$ mm) as the working electrode, a Pt wire as the counter electrode, and Hg/Hg$_2$Cl$_2$ (saturated KCl) as the reference electrode. Prior to use, the GCE was carefully polished with alumina paste for 30 s, thoroughly cleaned and air-dried. A catalyst dispersion was prepared by mixing it with ethanol. For cyclic voltammogram measurements, the catalyst dispersion was dropped onto the GCE electrode with a Pt loading of 26 μg/cm^2. After solvent evaporation, 2 μL of 0.05 wt% Nafion solution were dropped onto the surface of the GCE and air-dried. Before data collection, each catalyst-modified electrode was cleaned and activated in a 1.0 M KOH solution in the voltage range −0.85 to 0.25 V for at least 50 cycles until a stable CV was recorded. Cyclic voltammetry was first conducted at 50 mV/s in 1.0 M KOH solution within the potential range −0.85 to 0.25 V. MOR measurements of the catalysts were conducted in a solution containing 1.0 M KOH and 1.0 M CH$_3$OH at a scan rate of 50 mV/s within the potential range −0.8 to 0.25 V. Chronoamperometric (CA) curves were generated at −0.2 V in a solution containing 1.0 M KOH and 1.0 M CH$_3$OH for 3600 s to test the stabilities of various catalysts. The system was deaerated with N$_2$ before the voltammetric behavior was monitored.

Electrochemical CO-stripping voltammograms were recorded by oxidizing pre-adsorbed CO (CO$_{ad}$) in 0.5 M H$_2$SO$_4$ at a scan rate of 50 mV s^{-1}. CO was purged into 0.5 M H$_2$SO$_4$ for 30 min to allow complete adsorption of CO onto the deposit. The amount of CO adsorbed was evaluated by integrating the CO$_{ad}$ stripping peak and correcting for the capacitance of the double electric layer. The electrochemically active surface area (ECSA) of the catalyst was calculated based on the following equation [28, 29]:

$$ECSA = Q \big/ (m \times C),$$

where Q is the charge needed for CO desorption electrooxidation, m is the total metal loading of Pt and Pd on the working electrode, and C (420 μC cm^{-2}) is the charge needed for the oxidation of a CO monolayer on the catalyst. The detailed evaluation method used in this work can be found in S6 of the "Electronic supplementary material" (ESM).

Results and discussion

Characterization of the Pd-Pt nanocrystals

The morphology and structure of each as-prepared sample were characterized by TEM. Figure 1a shows typical TEM images of the as-prepared Pd-Pt octahedral nanocrystals, indicating that the obtained products were well dispersed and had complete octahedral nanostructures. The nanocrystals were highly uniform, with a narrow size range of 10 ± 2 nm. Thereafter the sample was characterized by high-resolution TEM (HRTEM) to obtain further insights into the structures of these nanocrystals. The clear lattice fringes had the same orientation. The d spacing of the adjacent lattice fringes is 0.23 nm, which can be assigned to the fcc (111) plane of the Pd-Pt metallic nanocrystals (Fig. 1b). In addition, both the HRTEM and the corresponding Fourier transform (FT) pattern (inset in Fig. 1b) applied to an individual Pt nanocrystal confirmed the single-crystalline nature of the Pd-Pt nanoarchitecture. The Pd-Pt nanostructure was further visualized by high-angle annular dark-field scanning TEM (HAADF-STEM) (Fig. 1d). Elemental mapping revealed that Pd and Pt elements were uniformly distributed throughout the nanostructures, confirming that homogeneous Pd-Pt alloy nanostructures were formed (Fig. 1d–g). Moreover, the compositional line scanning profiles further demonstrated this homogeneous distribution (Fig. 1c) and the formation of a Pt-Pd solid-solution alloy [12].

Energy-dispersive X-ray analysis (EDX) was used to determine the compositions of the samples (S1 in the ESM). The atomic ratio of Pd to Pt was determined as 1:1; this result agrees with the results of inductively coupled plasma optical emission spectrometry (ICP-OES) as well as the mole ratio of the precursors added (see S4 in the ESM).

The mole ratio of precursors is often a major influence on the morphology and structure of the product [30, 31]. In this work, Pd-Pt was prepared with different compositions by adjusting the mole ratio of the precursors (Pd:Pt = 1:2 and 1:3). As shown by TEM imaging (Fig. 2), the average nanocrystal size is not strongly influenced by the Pd:Pt ratio of the precursors. In both reaction systems the products were well dispersed and had complete octahedral nanostructures with a uniform size of approximately 10 ± 2 nm. In addition, both samples were single-crystalline and showed high crystallinity, as confirmed by the corresponding FFT pattern.
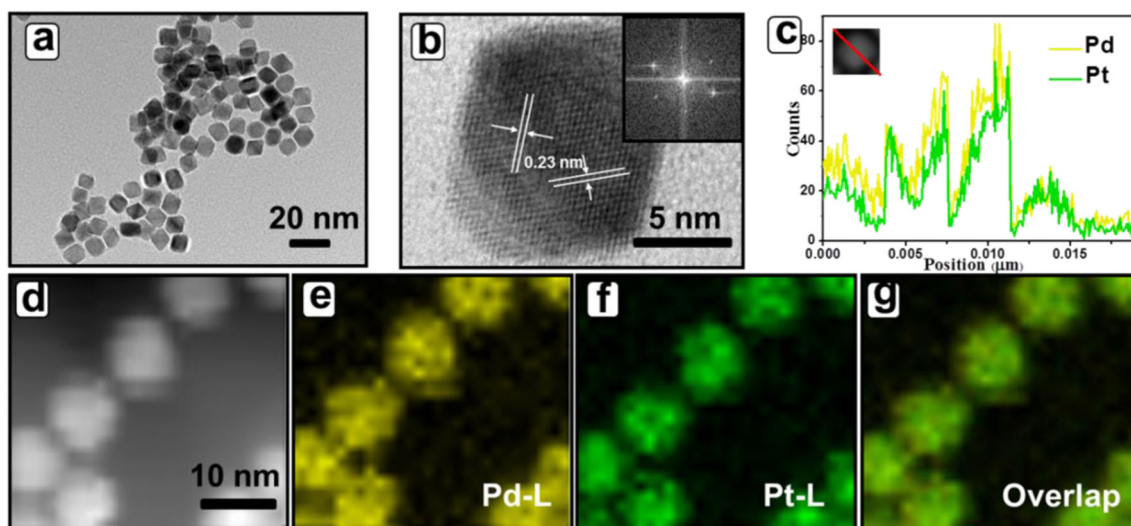
Fig. 1 **a** Typical TEM image of the prepared Pd_1Pt_1 bimetallic nanocrystals. **b** High-resolution TEM image and the corresponding FFT pattern (*inset*). **c–g** HAADF-STEM-EDS mapping images and line scanning profiles of the Pd_1Pt_1 bimetallic nanocrystals

Corresponding EDX and ICP-OES analyses of the bimetallic nanocrystals were performed, and are presented in Figs. S2 and S4 of the ESM. The results of the latter are in complete agreement with those of the former, which suggests that the reactions were performed without any loss of the metal precursors. Therefore, the products of both systems were denoted Pd_1Pt_2 and Pd_1Pt_3.

HAADF-STEM and elemental mapping of Pd_1Pt_3 indicated that Pd and Pt were uniformly distributed throughout the nanostructures, further confirming the formation of homogeneous Pd-Pt alloy nanostructures by the hydrothermal reaction method (see S3 in the ESM).

The wide-angle XRD profile of the Pd-Pt bimetallic nanocrystals was determined to further check their alloyed fcc crystal nanostructures (Fig. 3) [32, 33]. In the XRD spectra, the representative diffraction peaks at 39.9°, 46.4°, 67.6°, 81.6°, and 86.4° were assigned to the (111), (200), (220), (311), and (222) diffractions of a typical single-phase fcc crystal structure, respectively, which is consistent with the FFT pattern. As indicated in Fig. 3, the XRD peaks for the octahedral Pt-Pd nanocrystals shifted to higher 2θ values as the amount of Pd was increased; that is, there were (111) diffraction peaks at 39.98°, 40.02°, and 40.06° corresponding to Pd_1Pt_3, Pd_1Pt_2, and Pd_1Pt_1 nanocrystals, respectively, which

suggest that there was well-defined alloy formation between Pt and Pd [34].

X-ray photoelectron spectroscopy (XPS) was employed to examine the chemical states of the Pd-Pt bimetallic nanocrystals. Figure 4a and b show the Pt $4f$ and Pd $3d$ core-level spectra of individual Pd-Pt bimetallic nanocrystals; it is apparent that both of them include two sets of peaks. One set shows Pd $3d_{5/2}$ at 335.8 eV, Pd $3d_{3/2}$ at 340.9 eV, Pt $4f_{7/2}$ at 71.4 eV, and Pt $4f_{5/2}$ at 74.7 eV; these values are in good accord with those for Pd^0 and Pt^0, respectively [16, 35]. The other set includes Pd $3d_{5/2}$ at 336.6 eV, Pd $3d_{3/2}$ at 342.1 eV, Pt $4f_{7/2}$ at 72.0 eV, and Pt $4f_{5/2}$ at 75.7 eV, which are close to the reported values for Pd^{II} and Pt^{II}, respectively [16, 35, 36]. In terms of peak intensity, Pt^0 and Pd^0 are the predominant species. The complete reduction of $PtCl_6^{2-}$ and $PdCl_4^{2-}$ in the present synthesis process is revealed. Furthermore, the compositions of the Pd-Pt bimetallic nanocrystals were also confirmed by XPS (Table 1 in S4 of the ESM). The contents of Pt and Pd in the samples agree with the Pd:Pt ratio in the metal precursors used during the synthesis.
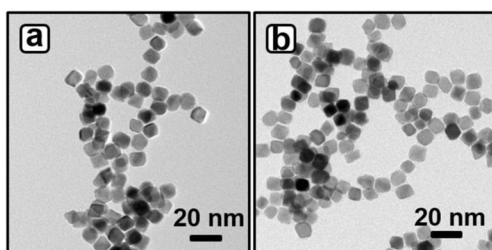

Fig. 2a–b TEM images of the other types of Pd-Pt nanocrystals with different compositions: **a** Pd_1Pt_2 and **b** Pd_1Pt_3
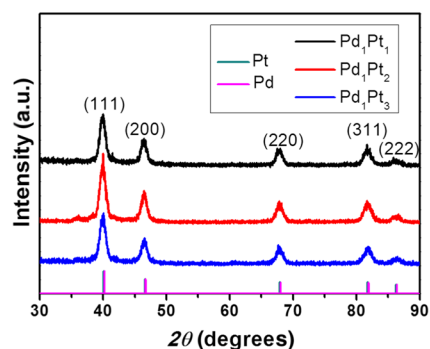

Fig. 3 XRD patterns of Pd-Pt alloy nanocrystals with different compositions: Pd_1Pt_1, Pd_1Pt_2, and Pd_1Pt_3

Fig. 4a–f Surface and chemical analysis by XPS. Pt 4*f* spectra in **a** Pd$_1$Pt$_1$, **b** Pd$_1$Pt$_2$, **c** Pd$_1$Pt$_3$. Pd 3*d* spectra in **d** Pd$_1$Pt$_1$, **e** Pd$_1$Pt$_2$, **f** Pd$_1$Pt$_3$. Comparison of chemical states and ratios of Pt 4*f* and Pd 3*d* spectra for all of the catalysts, measured and calculated from the XPS fitting data
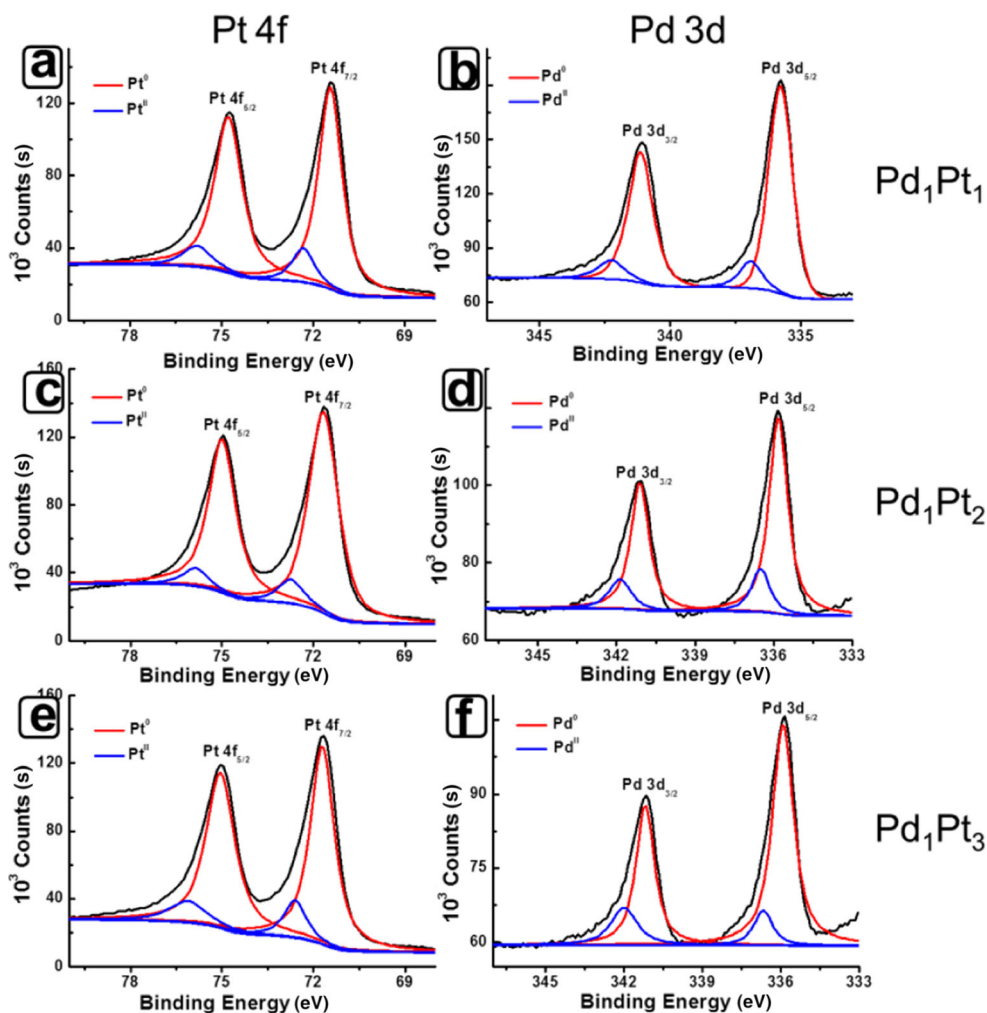
Formation mechanism of Pd-Pt nanocrystals

Clearly, both glucose and CTAB play critical roles in the formation of octahedral Pd-Pt nanocrystals. A series of control experiments was conducted to determine the influence of glucose and CTAB on the morphology of the final products. The influence of glucose was investigated first. As shown in Fig. 5a, in the absence of glucose, no octahedral nanocrystals were obtained, only those with large sizes and mixed morphologies, such as polyhedral structures and other irregular particles. When 0.25 M glucose was used, the products were significantly smaller, but the irregular particles continued to aggregate (Fig. 5b). As the glucose concentration was further increased to 0.5 M, uniform octahedral nanocrystals were seen (Fig. 1a). With a further increase in the concentration (1.0 M), no change in morphology was observed (Fig. 5c). On the other hand, as indicated in Fig. 5d, without the addition of CTAB to the synthetic system, large and small nanoparticles aggregated but none with octahedral morphology were formed. When the CTAB concentration was increased, the proportion of nanoparticles with a regular morphology gradually increased

(Fig. 5e and f). These findings show that both glucose and CTAB are essential for inducing the formation of octahedral bimetallic nanocrystals.

In order to investigate the morphological evolution of the octahedral Pd-Pt nanocrystals, aliquots of the reaction solution were collected at various stages and examined using electron microscopy. Figure 6 presents the TEM images of octahedral Pd-Pt nanocrystals collected periodically throughout the entire reaction. When the reaction time reached 10 min, the color of the reaction mixture changed from light yellow to light brown, and insignificant amounts of precipitate were obtained by centrifugation. However, the TEM image shows that large amounts of small, solid nanoparticles with sizes of less than 3 nm were obtained (Fig. 6a). The EDX results show that the product consists of Pt and Pd (Fig. 6a, inset). When the reaction time was increased to 20 min, the growth process was very quick: the small Pt particles rapidly disappeared and a number of octahedral Pd-Pt nanocrystals with an average size of 7 ± 2 nm appeared (Fig. 6b). However, within the TEM observation field, some octahedral Pd-Pt nanocrystals were still surrounded by some nanoparticles (see S5 in the ESM).
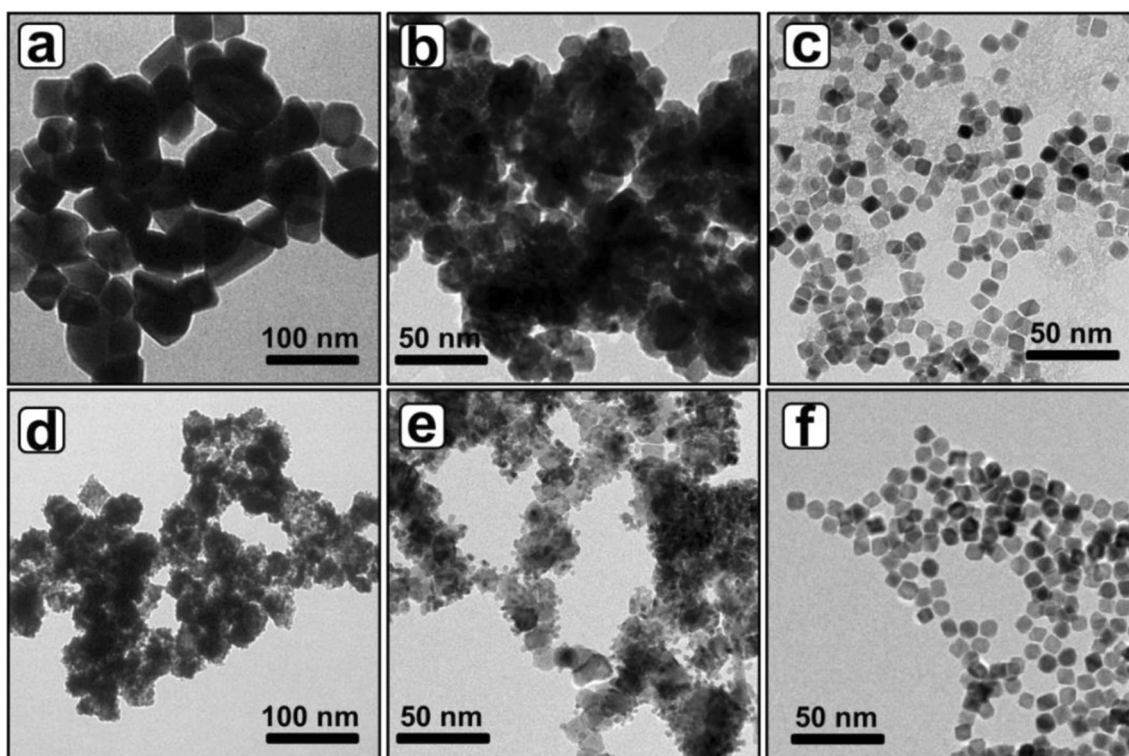
Fig. 5a–f Pd$_1$Pt$_1$ bimetallic nanocrystal morphologies obtained **a** without glucose, **b** with 0.25 M glucose, and **c** with 1.0 M glucose, and **d** without CTAB, **e** with 25 mM CTAB, and **f** with 50 mM CTAB are shown

As shown in Fig. 6c, when the reaction time was increased to 30 min, the nanoparticles disappeared completely, and the Pd-Pt nanocrystals expanded in size to 10 ± 1 nm. When the reaction time was further extended to 60 min, no significant change in either the size or surface structure was observed,
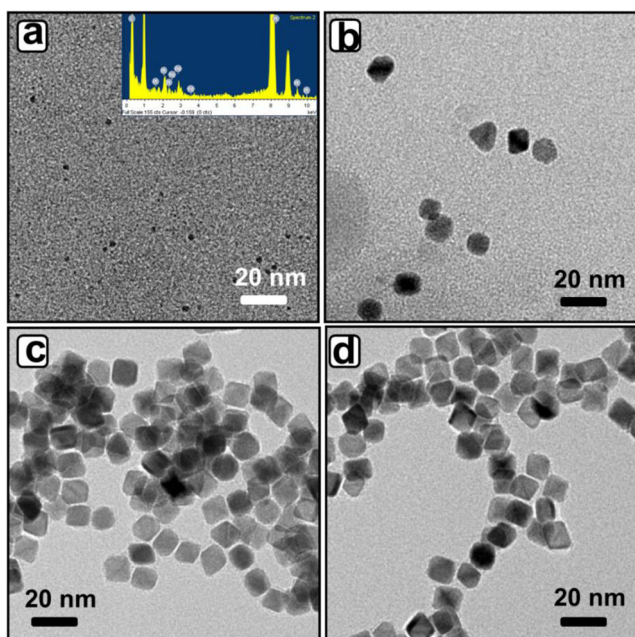

Fig. 6a–d TEM images of the samples collected at different reaction stages: **a** 10 min, **b** 20 min, **c** 30 min, and **d** 60 min

which, in combination with the EDX results, indicates that the reaction was completed within this time (Fig. 6d).

In general, two typical mechanisms were proposed to explain the formation of the single-crystalline nanocrystals. One was aggregation-based growth, in which a large number of nanoparticles are aggregated in a diffusion-controlled manner [37, 38], and the other was rapid growth, in which some small particles initially form as seeds and then rapidly grow into dendrites [39, 40]. Based on the TEM analysis, the formation of the octahedral Pd-Pt nanocrystals may follow the rapid-growth mechanism, which is described in detail in Scheme 1. At the earliest stage of the synthesis, a small number of seeds are formed. Thereafter, under the direct influence of the CTAB, a large number of atoms are absorbed and reduced on the seeds, leading to rapid crystal growth into the most stable octahedral structure with all (111) surfaces. Over time, the growth rate slows, and fully grown and stable Pd-Pt is formed after an hour.

Electrocatalytic measurements of the Pd-Pt electrocatalysts

Encouraged by their attractive properties, we tested the octahedral Pd-Pt bimetallic nanocrystals as electrocatalysts for MOR. Their catalytic activities were further benchmarked against commercially available Pt black and Pd black.

Scheme 1 Schematic illustration of the formation mechanism for octahedral Pd-Pt bimetallic nanocrystals
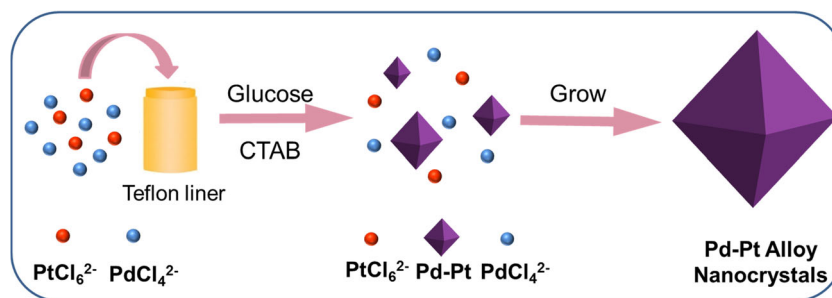
Cyclic voltammetry characterization of the Pd-Pt electrocatalysts in 1.0 M KOH

Cyclic voltammograms (CVs) of the catalyst-modified electrodes were recorded in 1.0 M KOH solution over the same potential range of −0.85 to 0.3 V, as displayed in Fig. 7. Clearly, all of the catalysts display well-defined hydrogen desorption/adsorption peaks and preoxidation/reduction peaks. In the positive scan, hydrogen desorption emerges in the potential window from −0.85 to −0.6 V, and hydroxyl (OH_{ad}) adsorption appears above −0.5 V. In the negative sweep, OH_{ad} reduction occurs from −0.5 to −0.1 V, and hydrogen adsorption occurs below −0.6 V. Evidently, the second H peak, which appears at −0.68 V for bare Pt, is suppressed for Pd_1Pt_1, Pd_1Pt_2, and Pd_1Pt_3. This is due to the adsorption of organic stabilizers on the surfaces of the metal nanoparticles, which is known to predominantly suppress the second H peak [11].

CO stripping voltammetry for the Pd-Pt electrocatalysts in 0.5 M H_2SO_4

Given that Pd is well known to be an excellent metal for adsorbing hydrogen, it does not make sense to derive the electrochemically active surface area (ECSA) of Pd-containing catalysts from the hydrogen region [41]. Thus, the ECSA of the Pd-Pt nanocomposite-modified electrode was calculated from CO-stripping measurements. The CO-
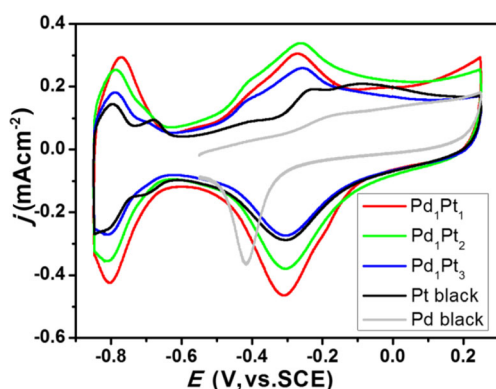

Fig. 7 CV curves of catalyst-modified GC electrodes in 1.0 M KOH solution; the scan rate was 50 mV/s

stripping voltammograms of the electrodes modified with Pd-Pt nanocomposites, Pt black, and Pd black in 0.5 M H_2SO_4 are shown in Fig. 8. The figure illustrates that the hydrogen desorption peaks were fully suppressed in the first positive scan because of the active sites occupied by the pre-adsorbed CO. The broad peak from 0.5 to 1.0 V is related to the oxidation of CO in the first scan. Hydrogen adsorption/desorption appears in the following sweep, and no CO oxidation is observed for any of the catalysts. Based on the assumption that the charge required for the oxidation of a CO monolayer on the catalyst is 420 μC/cm^2, the ECSA values of the catalysts were estimated using the accumulated electric charge of the CO desorption electrooxidation. The estimated ECSA values were found to be 77.0, 26.0, 26.0, 36.0, and 19.0 m^2/g for Pd_1Pt_1, Pd_1Pt_2, Pd_1Pt_3, Pt black, and Pd black, respectively (see S6 in the ESM). The ECSA of the Pd_1Pt_1 nanocrystals was greater than that of the commercial samples. The Pd_1Pt_1 bimetallic nanocrystals achieved the best electrocatalytic performance among these Pd-Pt nanocrystals with different Pd:Pt ratios.

Methanol oxidation on the Pt-Pd electrocatalysts in 1.0 M KOH

The typical MOR in alkaline media was chosen to demonstrate the electrocatalytic performance of the Pd-Pt nanocrystals. Electrooxidation of methanol was conducted in an aqueous solution containing 1.0 M KOH and 1.0 M methanol, using a cyclic voltammetry measurement technique sweeping from −0.8 to 0.25 V at a scan rate of 50 mV/s (Fig. 9a). The mass activity of the catalyst can be calculated using the current densities normalized by the total mass of Pt and Pd. For methanol oxidation, an oxidation peak was observed in the forward scan, corresponding to the oxidation of freshly chemisorbed methanol. This peak begins at about −0.7 V for the Pd-Pt catalysts, which, according to the CV in Fig. 8, corresponds to the beginning of Pd and Pt hydroxide formation. The current reaches a maximum value at about −0.15 V, after which the oxidation current decreases and reaches zero at a potential of 0.1 V, corresponding to the formation of a full Pd and Pt hydroxide layer. In the reverse sweep, another oxidation peak occurs over a significantly
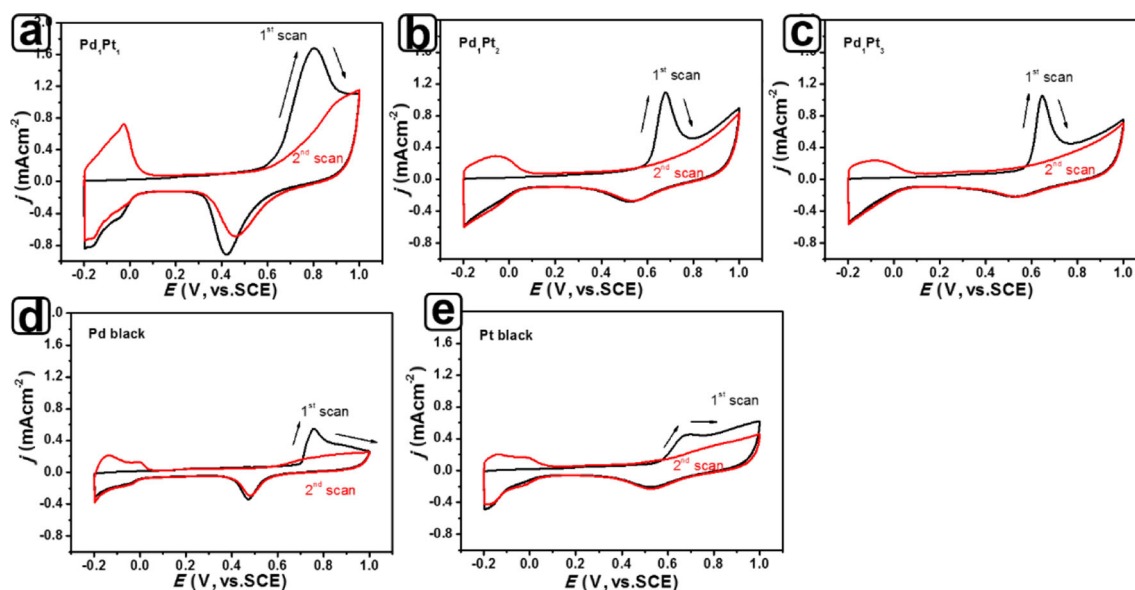
Fig. 8a–e CO-stripping voltammograms of electrodes modified with **a** Pd_1Pt_1, **b** Pd_1Pt_2, **c** Pd_1Pt_3, **d** Pd black, and **e** Pt black catalysts in 0.5 M H_2SO_4; the scan rate was 50 mV/s

narrower potential region and with a maximum current that is much lower than that seen in the anodic direction. This peak was attributed to the removal of carbonaceous species that were not completely oxidized in the forward scan. All of the Pd-Pt bimetallic samples showed excellent electrocatalytic methanol oxidation performance—better than commercial samples—which decreased in the order $Pd_1Pt_1 > Pd_1Pt_2 > Pd_1Pt_3$ at the first cycle. However, for fuel cell research, only steady-state activities are of interest, so the electrocatalytic activity and stability of the Pd-Pt bimetallic nanocrystals for the MOR were further investigated by chronoamperometry at −0.2 V for 3600 s in an aqueous solution containing 1.0 M KOH and 1.0 M methanol. The current densities of Pd_1Pt_3 were higher than those of Pd-Pt alloy samples and commercial samples over the entire time period (Fig. 9b), confirming that the electrocatalytic activities of the bimetallic nanocrystals decrease in the order $Pd_1Pt_3 > Pd_1Pt_2 > Pd_1Pt_1$, although all

of the nanocrystals performed better than the commercial samples.

The onset potential (E_{onset}) is commonly used as an indicator to compare the intrinsic activities of Pt and Pd for the MOR. However, a precise comparison of the E_{onset} values on catalysts is difficult to achieve; therefore, following [42], we used the half-wave potential ($E_{1/2}$) of the MOR to perform the comparison in this study. Results revealed that the $E_{1/2}$ on Pt black (−0.35 V) is evidently lower than that on Pd black (−0.25 V), indicating that Pt is intrinsically more active than Pd for the MOR. Furthermore, the $E_{1/2}$ shifts to lower potentials with increasing Pt content (Pd_1Pt_1: −0.26 V, Pd_1Pt_2: −0.30 V, and Pd_1Pt_3: −0.46 V), especially for Pd_1Pt_3, which showed the highest negative shift at approximately 121 mV (Pt black) and 215 mV (Pd black). This outcome indicates that the MOR on Pt is kinetically more facile than it is on Pd.
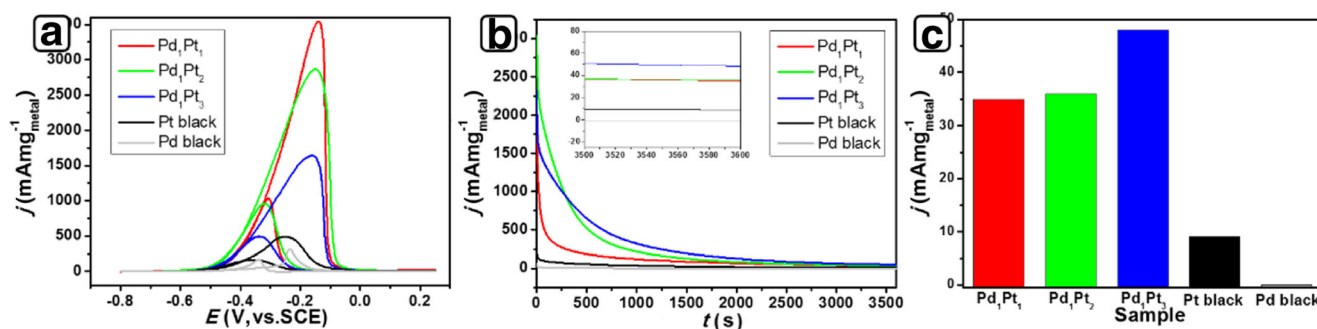

Fig. 9 **a** CV curves of catalyst-modified GC electrodes in 1.0 M KOH solution containing 1.0 M methanol at a scan rate of 50 mV/s. Mass activities are given as kinetic current densities (j) normalized by the loading amount of metal. **b, c** Chronoamperometric measurements of

the electrocatalytic activity of catalysts for the oxidation of methanol in 1.0 M KOH. Curves were obtained by measuring the current density under a constant potential of −0.2 V for 60 min

Furthermore, during the MOR, the Pt electrocatalysts lost a considerable amount of their catalytic activity due to the adsorption of CO-like carbonaceous species (CO_{ads}), unidentified non-CO_{ads} organic species, or both. The ratio of the forward oxidation current peak (I_f) to the reverse current peak (I_b), I_f/I_b, is an important index of the tolerance of the electrocatalysts to poisoning during the MOR [43]. A higher ratio indicates more effective removal of the poisoning species found on the electrocatalyst surface. All of the Pd-Pt bimetallic nanocrystals showed superior poison tolerance to the reference samples. The Pd_1Pt_3 nanocrystals exhibited the best poison tolerance; the I_f/I_b value was 3.4, which is significantly higher than those of the Pd_1Pt_1 (3.3) and Pd_1Pt_2 (3.1) nanocrystals as well as those of Pt black (2.9) and Pd black (1.9).

The durability of the electrode modified with Pd-Pt bimetallic nanocrystals was confirmed by cyclic voltammetry in 1.0 M KOH containing 1.0 M methanol (Fig. 10). The current density of the Pd_1Pt_1-modified electrode remained at 50 % and 39 % of its original value after 250 and 500 cycles, respectively; the current density of the Pd_1Pt_2-modified electrode remained at 67 % and 64 % of its original value after 250 and 500 cycles, respectively; and the current density of the Pd_1Pt_3-modified electrode remained at 65 % and 71 % of its original value after 250 and 500 cycles, respectively. These results demonstrate the high durability of the Pd_1Pt_3, which showed a slight increase in current density from 250 to 500 cycles. The high tolerance, improved electrocatalytic performance, and good stability of the samples can be attributed to synergistic effects between Pt and Pd. The evolution of the morphologies of the Pd-Pt bimetallic nanocrystal samples after 500 cycles was investigated by TEM to further understand their structural stabilities (see S7 in the ESM). All of the samples lost their original octahedral structure and connected to form dendritic structures. The Pd_1Pt_1 nanocrystals underwent severe aggregation. The Pd_1Pt_2 nanocrystals showed partial aggregation, whereas the Pd_1Pt_3 nanocrystals presented slight aggregation. Clearly, increasing the amount of Pt greatly improved the stability of the nanocrystals. This may be because,

during the long duration of the potential scan, the Pd nanoparticles undergo Ostwald ripening and aggregation to form larger particles due to the high surface energy of Pd, and the incorporation of Pt into Pd could delay the coarsening of its structure and inhibit the dissolution of Pd [44].

Based on the above discussions, we can conclude that although Pd is less active than Pt towards the MOR in alkaline solutions, combining these two metals leads to better catalytic activity than bare Pt, such that high Pt utilization can be achieved along with excellent catalytic activity. Pd_1Pt_3 appears to be the best electrocatalyst among all of the samples tested, considering its excellent electrocatalytic performance, onset potential, long-term stability, and durability. The high tolerance, improved electrocatalytic performance, and good stability of the Pd-Pt nanocrystals indicate a strong synergistic effect between Pd and Pt, which may be attributed to the following reasons. Firstly, the self-supported structures are stable, meaning that they can prevent severe corrosion [45, 46]. Secondly, for the MOR in alkaline media, the carbonate route is the dominant process; this involves the adsorption of CO as a poisoning intermediate [27]. The electronic effect caused by Pd and Pt may lower the binding energies of adsorbed reaction intermediates such as CO_{ads} or OH_{ads} species, thus facilitating the carbonate reaction pathway for methanol oxidation through the adsorption of oxygen-containing species [16, 47]. Thirdly, the moderate incorporation of Pd into Pt could delay the coarsening of the Pd structure, inhibit the dissolution of Pd, and enhance the electroactivity and durability of the catalysts.

Conclusions

In summary, we have successfully developed a facile, one-pot hydrothermal reduction method for the synthesis of bimetallic Pd-Pt octahedral nanocrystals with an alloyed structure. The as-prepared catalysts exhibited enhanced activity, long-term stability, and durability for methanol electrooxidation compared to commercial catalysts in alkaline conditions,
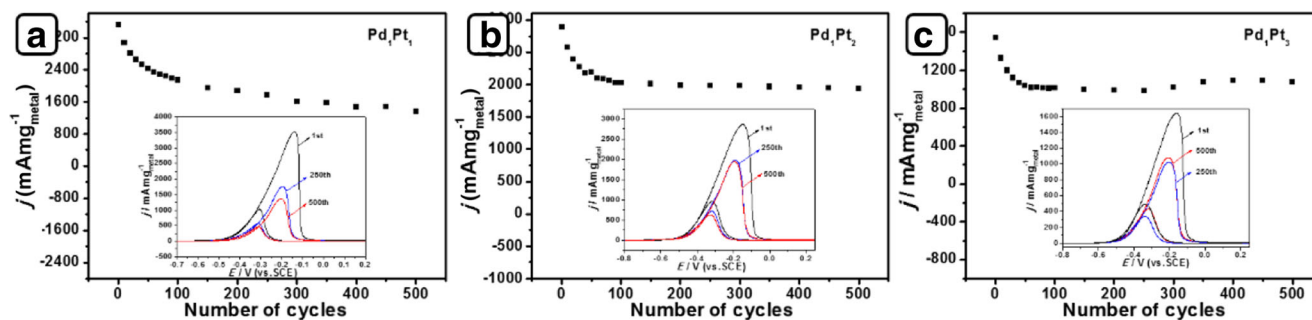

Fig. 10a–c Plots of the forward peak current densities (j) on the catalyst-modified electrodes (a Pd_1Pt_1, b Pd_1Pt_2, c Pd_1Pt_3) against the number of CV cycles performed in 1.0 M KOH containing 1.0 M methanol. *Insets* show the 1st, 250th, and 500th cyclic voltammograms obtained on each electrode at a scan rate of 50 mV/s

demonstrating that they can be used as effective electrocatalysts for direct methanol fuel cells. In addition, this simple method could also be generalized to produce other noble-metal-based bimetallic nanostructures for catalytic applications by changing the precursors used in the synthetic process. The as-synthesized catalysts may also find other applications in fuel cells, such as formic acid oxidation, methanol oxidation, oxygen reduction reaction, and others, because of their convenient preparation.

References

1. Wang W, Wang D, Liu X, Liu X, Peng Q, Li Y (2013) Pt–Ni nanodendrites with high hydrogenation activity. Chem Commun 49:2903–2905

2. Chen A, Holt-Hindle P (2010) Platinum-based nanostructured materials: synthesis, properties, and applications. Chem Rev 110: 3767–3804

3. Wu B, Zheng N, Fu G (2011) Small molecules control the formation of Pt nanocrystals: a key role of carbon monoxide in the synthesis of Pt nanocubes. Chem Commun 47:1039–1041

4. Lv J, Zheng J, Li S, Chen L, Wang A, Feng J (2014) Facile synthesis of Pt-Pd nanodendrites and their superior electrocatalytic activity. J Mater Chem A 2:4384–4390

5. Mazumder V, Chi M, More KL, Sun S (2010) Core/shell Pd/FePt nanoparticles as an active and durable catalyst for the oxygen reduction reaction. J Am Chem Soc 132:7848–7849

6. Guo S, Li J, Dong S, Wang E (2010) Three-dimensional Pt-on-Au bimetallic dendritic nanoparticle: one-step, high-yield synthesis and its bifunctional plasmonic and catalytic properties. J Phys Chem C 114:15337–15342

7. Lu N, Wang J, Xie S, Brink J, Mcllwrath K, Xia Y, Kim MJ (2014) Aberration corrected electron microscopy study of bimetallic Pd–Pt nanocrystal: core-shell cubic and core-frame concave structures. J Phys Chem C 118:28876–28882

8. Xie S, Choi S, Lu N, Roling LT, Herron JA, Zhang L, Park J, Wang J, Kim MJ, Xie Z, Mavrikakis M, Xia Y (2014) Atomic layer-by-layer deposition of Pt on Pd nanocubes for catalysts with enhanced activity and durability toward oxygen reduction. Nano Lett 14: 3570–3576

9. Matin MA, Jang JH, Kwon YU (2014) One-pot sonication-assisted polyol synthesis of trimetallic core-shell (Pd, Co)@Pt nanoparticles for enhanced electrocatalysis. Int J Hydrogen Energy 39:3710–3718

10. Gong M, Fu G, Chen Y, Tang Y, Lu T (2014) Autocatalysis and selective oxidative etching induced synthesis of platinum-copper bimetallic alloy nanodendrites electrocatalysts. ACS Appl Mater Interfaces 6:7301–7308

11. Wang S, Kuai L, Huang Y, Xue Y, Liu Y, Li W, Chen L, Geng B (2013) A highly efficient, clean-surface, porous platinum electrocatalyst and the inhibition effect of surfactants on catalytic activity. Chem-Eur J 19:240–248

12. Zhang H, Jin M, Xia Y (2012) Enhancing the catalytic and electro-catalytic properties of Pt-based catalysts by forming bimetallic nanocrystals with Pd. Chem Soc Rev 41:8035–8049

13. Xia B, Wu H, Wang X, Wen X, Lou X (2012) One-pot synthesis of cubic PtCu$_3$ nanocages with enhanced electrocatalytic activity for the methanol oxidation reaction. J Am Chem Soc 134:13934–13937

14. Ataee-Esfahani H, Imura M, Yamauchi Y (2013) All-metal mesoporous nanocolloids: solution-phase synthesis of core-shell Pd@Pt nanoparticles with a designed concave surface. Angew Chem Int Ed 52:13611–13615

15. Wang L, Yamauchi Y (2013) Metallic nanocages: synthesis of bimetallic Pt-Pd hollow nanoparticles with dendritic shells by selective chemical etching. J Am Chem Soc 135:16762–16765

16. Liu W, Rodriguez P, Borchardt L, Foelske A, Yuan J, Herrmamm A, Geiger D, Zheng Z, Kaskel S, Gaponik N, Kötz R, Schmidt TJ, Eychmüller A (2013) Bimetallic aerogels: high-performance electrocatalysts for the oxygen reduction reaction. Angew Chem Int Ed 52:9849–9852

17. Mednikov EG, Jewell MC, Dahl LF, Mednikov EG, Jewell MC, Dahl LF (2007) Nanosized (μ_{12}-Pt)Pd$_{164-x}$ Pt$_x$(CO)$_{72}$(PPh$_3$)$_{20}$ ($x \approx 7$) containing Pt-centered four-shell 165-atom Pd-Pt core with unprecedented intershell bridging carbonyl ligands: comparative analysis of icosahedral shell-growth patterns with geometrically related Pd$_{145}$(CO)$_x$(PEt$_3$)$_{30}$ ($x \approx 60$) containing capped three-shell Pd$_{145}$ core. J Am Chem Soc 129:11619–11630

18. Yin A, Min X, Zhang Y, Yan C (2011) Shape-selective synthesis and facet-dependent enhanced electrocatalytic activity and durability of monodisperse sub-10 nm Pt-Pd tetrahedrons and cubes. J Am Chem Soc 133:3816–3819

19. Zhang Z, Hui J, Guo Z, Yu Q, Xu B, Zhang X, Liu Z, Xu C, Gao J, Wang X (2012) Solvothermal synthesis of Pt-Pd alloys with selective shapes and their enhanced electrocatalytic activities. Nanoscale 4:2633–2639

20. Lim B, Jiang M, Camargo P, Cho E, Tao J, Lu X, Zhu Y, Xia Y (2009) Pd-Pt bimetallic nanodendrites with high activity for oxygen reduction. Science 324:1302–1305

21. Choi I, Ahn SH, Kim JJ, Kwon OJ (2011) Preparation of Pt$_{shell}$–Pd$_{core}$ nanoparticle with electroless deposition of copper for polymer electrolyte membrane fuel cell. Appl Catal B 102:608–613

22. Koenigsmann C, Santulli AC, Gong K, Vukmirovic MB, Zhou W, Sutter E, Wong SS, Adzic RR (2011) Enhanced electrocatalytic performance of processed, ultrathin, supported Pd–Pt core-shell nanowire catalysts for the oxygen reduction reaction. J Am Chem Soc 133:9783–9795

23. Yu EH, Scott K, Reeve RW (2003) A study of the anodic oxidation of methanol on Pt in alkaline solutions. J Electroanal Chem 547:17–24

24. Spendelow JS, Wieckowski A (2007) Electrocatalysis of oxygen reduction and small alcohol oxidation in alkaline media. Phys Chem Chem Phys 9:2654–2675

25. Jing M, Jiang L, Yi B, Sun G (2013) Comparative study of methanol adsorption and electro-oxidation on carbon-supported platinum in acidic and alkaline electrolytes. J Electroanal Chem 688: 172–179

26. Kadirgan F, Beden B, Leger JM, Lamy C (1981) Synergistic effect in the electrocatalytic oxidation of methanol on platinum + palladium alloy electrodes. J Electroanal Chem 125:89–103

27. Maksic A, Rakocevic Z, Smiljanic M, Nenadovic M, Strbac S (2015) Methanol oxidation on Pd/Pt(poly) in alkaline solution. J Power Sources 273:724–734

28. Li S-S, Zheng J-N, Ma X, Hu Y-Y, Wang A-J, Chen J-R, Feng J-J (2014) Facile synthesis of hierarchical dendritic PtPd nanogarlands supported on reduced graphene oxide with enhanced electrocatalytic properties. Nanoscale 6:5708–5713

29. Lu Y, Jiang Y, Wu H, Chen W (2013) Nano-PtPd cubes on graphene exhibit enhanced activity and durability in methanol electrooxidation after CO stripping-cleaning. J Phys Chem C 117: 2926–2938

30. Mohanty A, Garg N, Jin R (2010) A universal approach to the synthesis of noble metal nanodendrites and their catalytic properties. Angew Chem Int Ed 49:4962–4966

31. Neppolian B, Sáez V, González-García J, Grieser F, Gómez R, Ashokkumar M (2014) Sonochemical synthesis of graphene oxide supported Pt-Pd alloy nanocrystals as efficient electrocatalysts for methanol oxidation. J Solid State Electrochem 18:3163–3171

32. Gong K, Park J, Su D, Adzic RR (2014) Metalizing carbon nanotubes with Pd–Pt core–shell nanowires enhances electrocatalytic activity and stability in the oxygen reduction reaction. J Solid State Electrochem 18:1171–1179

33. Limpattayanate S, Hunsom M (2013) Effect of supports on activity and stability of Pt–Pd catalysts for oxygen reduction reaction in proton exchange membrane fuel cells. J Solid State Electrochem 17:1221–1231

34. Lee YW, Ko AR, Kim DY, Han SB, Park KW (2012) Octahedral Pt-Pd alloy catalysts with enhanced oxygen reduction activity and stability in proton exchange membrane fuel cells. RSC Adv 2: 1119–1125

35. Veisz B, Tóth L, Teschner D, Paál Z, Gy rffy N, Wild U, Schlögl R (2005) Palladium-platinum powder catalysts manufactured by colloid synthesis: I. Preparation and characterization. J Mol Catal A 238:56–62

36. Yamamoto K, Imaoka T, Chun WJ, Enoki O, Katoh H, Takenaga M, Sonoi A (2009) Size-specific catalytic activity of platinum clusters enhances oxygen reduction reactions. Nat Chem 1:397–402

37. Banfield JF, Welch SA, Zhang H, Ebert TT, Penn RL (2000) Aggregation-based crystal growth and microstructure development in natural iron oxyhydroxide biomineralization products. Science 289:751–754

38. Liao H, Cui L, Whitelam S, Zheng H (2012) Real-time imaging of Pt_3Fe nanorod growth in solution. Science 336:1011–1014

39. Wang F, Li C, Sun LD, Xu CH, Wang J, Yu JC, Yan CH (2012) Porous single-crystalline palladium nanoparticles with high catalytic activities. Angew Chem Int Ed 51:4872–4876

40. Watt J, Cheong S, Toney MF, Ingham B, Cookson J, Bishop PT, Tilley RD (2009) Ultrafast growth of highly branched palladium nanostructures for catalysis. ACS Nano 4:396–402

41. Zheng J-N, Li S-S, Ma X, Chen F-Y, Wang A-J, Chen J-R, Feng J-J (2014) Green synthesis of core-shell gold-palladium@palladium nanocrystals dispersed on graphene with enhanced catalytic activity toward oxygen reduction and methanol oxidation in alkaline media. J Power Sources 262:270–278

42. Waszczuk P, Barnard TM, Rice C, Masel RI, Wieckowski A (2002) A nanoparticle catalyst with superior activity for electrooxidation of formic acid. Electrochem Commun 4:599–603

43. Zhang Y, Janyasupab M, Liu C, Li X, Xu J, Liu C (2012) Three dimensional PtRh alloy porous nanostructures: tuning the atomic composition and controlling the morphology for the application of direct methanol fuel cells. Adv Funct Mater 22:3570–3575

44. Chu Y-Y, Wang Z-B, Jiang Z-Z, Gu D-M, Yin G-P (2012) Facile synthesis of hollow spherical sandwich PtPd/C catalyst by electrostatic self-assembly in polyol solution for methanol electrooxidation. J Power Sources 203:17–25

45. Wang YJ, Wilkinson DP, Zhang J (2011) Noncarbon support materials for polymer electrolyte membrane fuel cell electrocatalysts. Chem Rev 111:7625–7651

46. Antolini E (2009) Carbon supports for low-temperature fuel cell catalysts. Appl Catal B Environ 88:1–24

47. Liu L, Pippel E, Scholz R, Gosele U (2009) Nanoporous Pt-Co alloy nanowires: fabrication, characterization, and electrocatalytic properties. Nano Lett 9:4352–4358